

Nanoscale Pattern Decay Monitored Line-by-Line *via in-situ* Heated

AFM

Sonal Bhadauriya¹, Jianan Zhang², Jaejun Lee², Michael R. Bockstaller², Alamgir Karim^{1,3}

*Richard J. Sheridan^{*4}, Christopher M. Stafford^{*4}*

¹Department of Polymer Engineering, University of Akron, Akron, Ohio 44325, United States

²Department of Materials Science and Engineering, Carnegie Mellon University, Pittsburgh,
Pennsylvania 15213, United States

³Department of Chemical and Biomolecular Engineering, University of Houston, Houston, Texas
77204, United States

⁴Materials Science and Engineering Division, National Institute of Standards and Technology,
Gaithersburg, Maryland 20899, United States

Keywords: atomic force microscopy; patterns; relaxation; in-situ; nanocomposites; polymers;
thin films

Abstract

We combine *in-situ* heated atomic force microscopy (AFM) with automated line-by-line spectral analysis to quantify the relaxation or decay phenomenon of nanopatterned composite polymer films above the glass transition temperature of the composite material. This approach enables assessment of pattern fidelity with a temporal resolution of ≈ 1 s, providing the necessary data density to confidently capture the short time relaxation processes inaccessible to conventional *ex-situ* measurements. Specifically, we studied the thermal decay of nanopatterned polymethylmethacrylate (PMMA) and PMMA nanocomposite films containing unmodified and PMMA-grafted silica nanoparticles (SiO_2 NP) of varying concentrations and film thicknesses using this new approach. Features imprinted on neat PMMA films were seen to relax at least an order of magnitude faster than the NP filled films at decay temperatures above the glass transition of the PMMA matrix. It was also seen that patterned films with the lowest residual thickness (34 nm) filled with unmodified SiO_2 NP decayed the slowest. The effect of nanoparticle additive was almost negligible in reinforcing the patterned features for films with the highest residual thickness (257 nm). Our *in-situ* pattern decay measurement and the subsequent line-by-line spectral analysis enabled the investigation of various parameters affecting the pattern decay such as the underlying residual thickness, type of additive system, and the exposure temperature in a timely and efficient manner.

Introduction

Patterned polymeric surfaces are ubiquitous, typically arising in smart coatings^{1,2}, biomimetic sensors³, microfluidic devices⁴, optical diffusers and gratings⁵, and during nano-device fabrication⁶⁻⁹. The nanofeatures imprinted on such patterned homopolymer¹⁰⁻¹² and composite¹³ films are known to decay *via* Laplace pressure driven viscous flow coupled with residual stresses¹⁴.

Understanding and characterizing the pattern fidelity precisely and accurately in a non-destructive manner, under various stimuli, is an important aspect to consider from an application standpoint. Miniaturization of electronic devices can lead to poor thermal management inside the device¹⁵ requiring robust pattern fidelity characterization as a function of time and temperature. Cross-sectional scanning electron microscopy (SEM) has been routinely used to check for pattern defects after imprinting^{16,17}. This technique requires the sample be destroyed to facilitate measurement (breaking/cutting the sample to visualize the film thickness and pattern dimensions in cross section) and the scope for dynamic measurements (such as with thermal exposure) is limited. Specular X-ray reflectivity¹⁸ and critical dimension small-angle X-ray scattering (CD-SAXS)¹⁹⁻²⁴ have also been used for static and stimulus-driven measurements of pattern fidelity, shape features, and line edge roughness. These techniques are less destructive to the sample but require model fitting to interpret the acquired data, as they do not provide a direct representation of the sample topography.

Nanostructure decay for homopolymer and composite films have been investigated *ex-situ via* direct topographic measurement (AFM)^{10,13,25}, sometimes in combination with SEM¹¹. *Ex-situ* techniques require a large number of samples and a large time investment to fully characterize the system. For example, to quantify the relaxation dynamics of two imprinted nanoparticle composite systems at five exposure temperatures, four nanoparticle concentrations (plus one control), three residual layer thicknesses with at least seven individual data points in each of the decay curves (for fitting a relaxation function) would require a total of ≈ 900 samples to be imaged via AFM. At roughly (4 to 8) min of scan time per image *via ex-situ* AFM (dependent on scan rate and aspect ratio), it would require approximately (60 to 120) h to fully characterize the topographic height decay of that system. Therefore, robust *in-situ* decay measurements are sought for better sample

economics and time management. *In-situ* measurements of pattern decay have previously been explored *via* ellipsometry (scatterometry)²⁶, light scattering¹⁴, and CD-SAXS²⁷. Here, we present an efficient *in-situ* approach using heated AFM to monitor the real time topography of decaying patterned polymer features. The relaxation behavior was captured above the glass transition temperature of the matrix and the composite material ($T_{g, \text{PMMA matrix}} \approx 97.2 \text{ }^\circ\text{C}$, $T_{g, 20 \% \text{ grafted SiO}_2 \text{ NP}} \approx 99.7 \text{ }^\circ\text{C}$ and $T_{g, 20 \% \text{ bare SiO}_2 \text{ NP}} \approx 100.3 \text{ }^\circ\text{C}$; see SI for details). High-throughput, automated analysis of the surface topography data gives direct insight into the shape evolution and relaxation dynamics of the patterned films.

Results and Discussion

Parallel line and space patterns (height, H , $\approx 150 \text{ nm}$ and wavelength, L , $\approx 850 \text{ nm}$) were imprinted with a sawtooth cross sectional profile *via* capillary force lithography²⁸ using a soft elastomeric polydimethylsiloxane (PDMS) stamp as shown in Figure 1. Both neat PMMA and PMMA nanocomposite films (with 20 % mass fraction of bare silica nanoparticles ($\text{SiO}_2 \text{ NP}$) and 20 % mass fraction of PMMA-grafted $\text{SiO}_2 \text{ NP}$ relative to the matrix mass) were investigated. The molecular mass of the PMMA matrix is 3 kg/mol with a polydispersity of 1.09. The average radius of the bare $\text{SiO}_2 \text{ NP}$ was $4.5 (\pm 0.5) \text{ nm}$. PMMA grafted $\text{SiO}_2 \text{ NP}$ had an average radius of $7.7 (\pm 2) \text{ nm}$ after grafting and the number average molecular mass (M_n) of the grafted chains was 19.4 kg/mol with a grafting density $\approx 0.65 \text{ chains/nm}^2$. After imprinting, the underlying non-patterned part of the film (“residual thickness or residual layer” as shown in Figure 1 as h_R) plays a significant role in affecting the decay phenomenon of the pattern¹⁰; therefore, different residual thickness of $\approx 34 \text{ nm}$, $\approx 152 \text{ nm}$, and $\approx 257 \text{ nm}$ were also investigated *via* this technique.

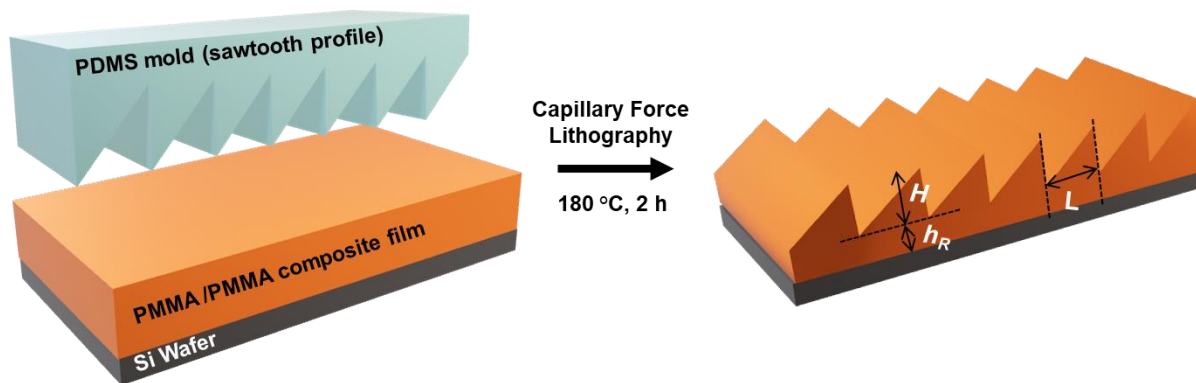


Figure 1. Schematic illustrating the capillary force lithography process used to produce patterned PMMA and the PMMA composite films. A soft elastomeric PDMS mold is brought in contact with a blade-coated film, and the assembly is heated above the T_g of the PMMA matrix to transfer the pattern via mold filling with high fidelity. The height, H , and the wavelength, L , of the sawtooth pattern is approximately 150 nm and 850 nm respectively, after imprinting. The residual layer, h_R depends on the thickness of the blade coated film before imprinting.

Figure 2 depicts how continuous scanning was translated into continuous capture of height decay for a patterned sample. The relevant AFM scan parameters were: scan rate = 1 Hz, scan size = 10 μm , aspect ratio = 1, and samples/line = 512. Therefore, a single AFM scan line was comprised of 512 data points in x (fast scan axis), which equates to a data spacing of roughly 20 nm and allows us to adequately capture the surface profile of the nanopattern. Additionally, each AFM image was comprised of 512 lines in y (slow scan axis), representing discrete time points in the decay process with a time resolution of 1 s (1 Hz). The AFM was run in “continuous capture” mode, meaning that when the AFM head reached the end of a scan, it would immediately reverse the scan direction and continue to scan the nanopatterned sample. We chose to operate in the “continuous capture” mode rather than disabling the slow scan axis (that is, repeatedly scan the same exact location on the sample) to reduce any potential tip-induced deformation of the pattern during imaging. Image capture continued until the pattern height trace reached ≈ 10 nm. For each

sample, we recorded the time required to place the sample on the AFM heat stage and subsequently engage the AFM head/tip onto the sample surface. This delay time was accounted for during the image analysis and was generally observed to be between 45 s and 90 s.

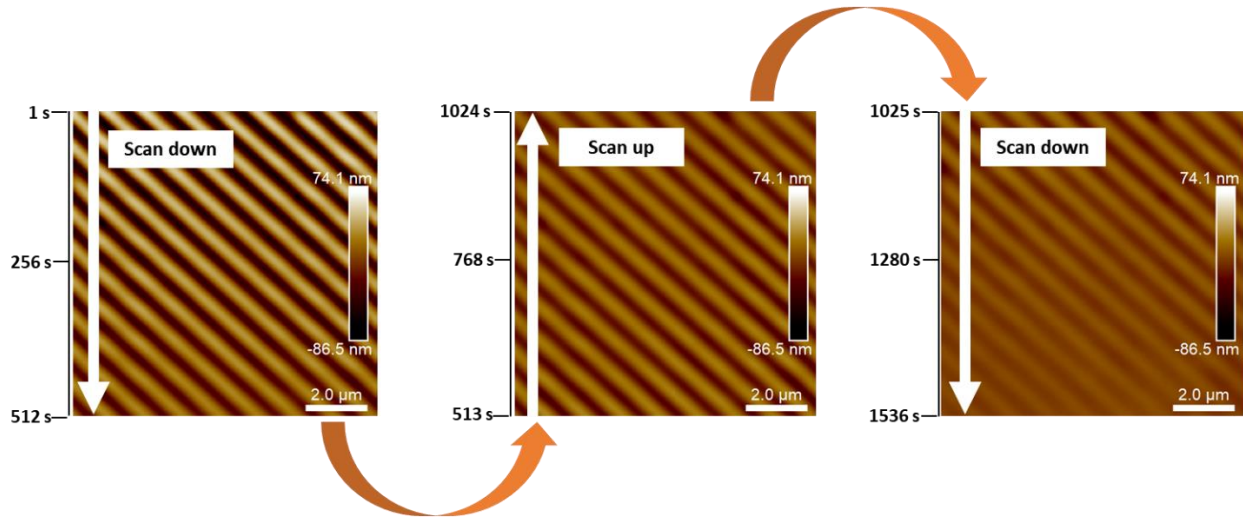


Figure 2. *In-situ* capture of pattern height decay for a neat PMMA film exposed to 120 °C ($h_R \approx 34$ nm) using heated AFM. Continuous scanning was employed with a scan resolution of 1 line/second.

One of the biggest advantages of this *in-situ* pattern decay measurement technique is the observation of direct shape evolution of the patterns as shown in Figure 3. As the patterns decay, each scan line becomes a discrete temporal data point, enabling us to directly observe the shape evolution from an initial *asymmetric* sawtooth profile into a *symmetric* sinusoidal profile, suggesting that a spectral analysis could be a robust choice for quantification. We compare the difference in shape evolution for a neat PMMA film and a nanocomposite film in Figure 3. The neat PMMA film decaying at 120 °C loses the sawtooth profile quite early during the decay process (as shown in Figures 3a and 3b), whereas the nanocomposite film holds onto the sawtooth profile and gradually loses the asymmetric line profile (Figures 3c and 3d), becoming sinusoidal later compared to the neat PMMA film. Similar shape evolution for rectangular gratings^{14,26} has been

shown before where the initial height decay is convoluted with a rounding of the rectangular edges, driving the gratings to become sinusoidal with time. We witness a similar polymer reflow at these sawtooth notches, where the initial height decay is coupled with rounding of the sharp notches, driving the line profile to become sinusoidal with time. Another important implication of the line profiles shown in Figures 3b and 3d is the relaxation of the imprinted features is much slower in composite films compared to the neat PMMA film. This slowing down of the relaxation time for composite films has been observed before in *ex-situ* experiments as discussed in our previous paper¹³.

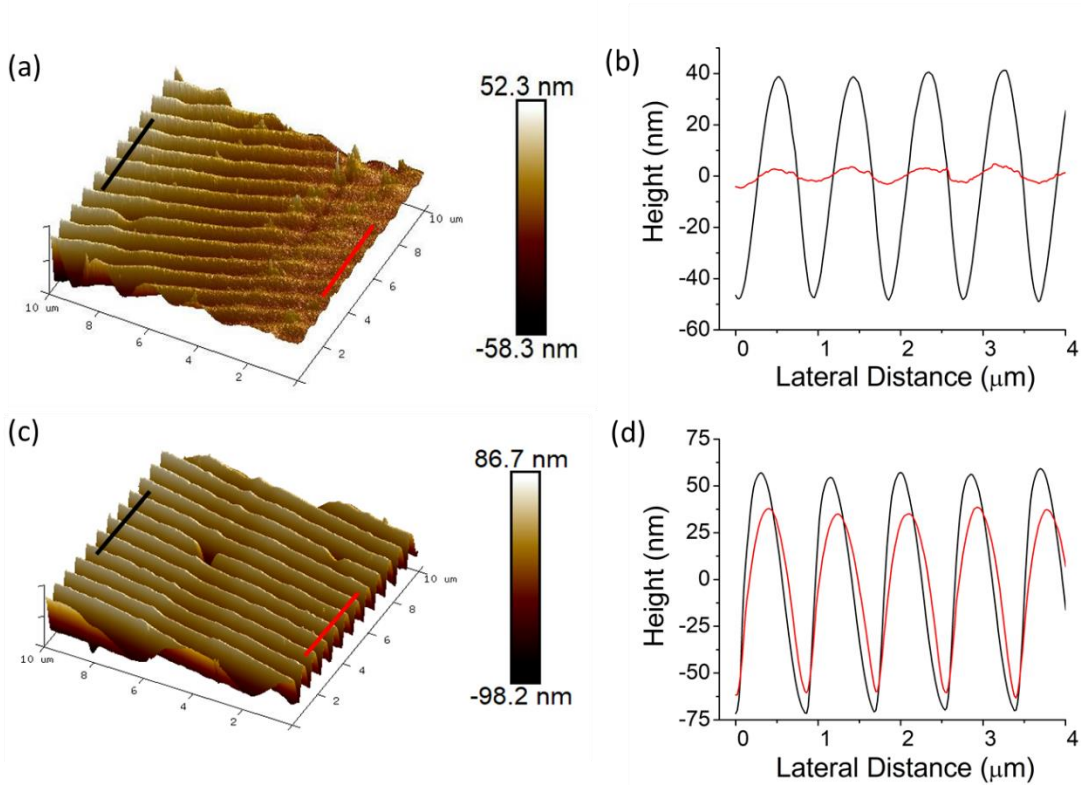


Figure 3. 3D AFM height image of the patterned film decaying at 120 °C with a h_R of 152 nm for (a) neat PMMA and (c) 20 % filled (w.r.t mass of PMMA matrix) bare SiO₂ NP film. Shape evolution of the features are depicted by line profiles shown in (b) and (d) where the time difference between the red and the black scan lines is approximately 500 s for both the samples.

Due to the periodicity of the imprinted pattern, a Fourier analysis was done for each scan line. Any periodic function can be described as a sum of sinusoidal waves:

$$s(x) = \sum_n A_n \sin(2\pi nx/L + \varphi_n) \dots \dots \dots (1)$$

where A_n is the n^{th} order Fourier mode amplitude, L is the pattern wavelength, and φ_n is the n^{th} order Fourier mode phase. The power spectrum of such a function will have regularly spaced peaks at each multiple of the fundamental spatial frequency, the amplitudes of which correspond to A_n . The evolution of these peaks over time provides a complete description of the nano pattern decay. A partial differential equation for thin films predicts²⁹ that, if the pattern is small in amplitude compared to the film thickness, each Fourier mode will relax independently of the others. Higher-order modes can play a significant role in defining the overall pattern relaxation for ultra-thin polymer films (with very low h_R), therefore tracking only the primary peak decay in that case might not be sufficient. For this study, our data generally meets the independent relaxation criterion for the higher-order modes as the abundance of influence on the fits comes from the tail of the relaxation curve which satisfies the small amplitude assumption. Therefore, we only consider the fundamental mode for all cases as a simplifying assumption.

Figure 4 depicts the spectral analysis and subsequent height decay of a representative patterned film of PMMA with 20 % mass fraction bare SiO₂ NP at 125 °C with $h_R = 152$ nm. Each scan line yields a temporally resolved “spectral average peak to peak (SPTP) amplitude” (see Experimental section). Figure 4a shows a sequential AFM height map for a patterned film where the decay can be easily visualized as function of time. Any defect arising in the pattern as shown in Figure 4a (for example feature distortion, dust particle, NP cluster etc.) does not bias the fit results as these lines are identified and masked prior to fitting (see experimental section). Figure 4b illustrates the resultant spectrogram exhibiting SPTP amplitude as a function of the spatial frequency of the

pattern signifying the sinusoidal nature of these patterns. Tracking the decay of the primary peak in Figure 4b can yield the decay curve of the pattern height as shown in Figure 4c. The decay curve is fitted to a stretched exponential function

$$A = A_0 e^{-\left(\frac{t}{\tau}\right)^\beta} \dots\dots\dots (2)$$

yielding the important physical parameters of the relaxation process, the decay time τ and the stretching parameter β .

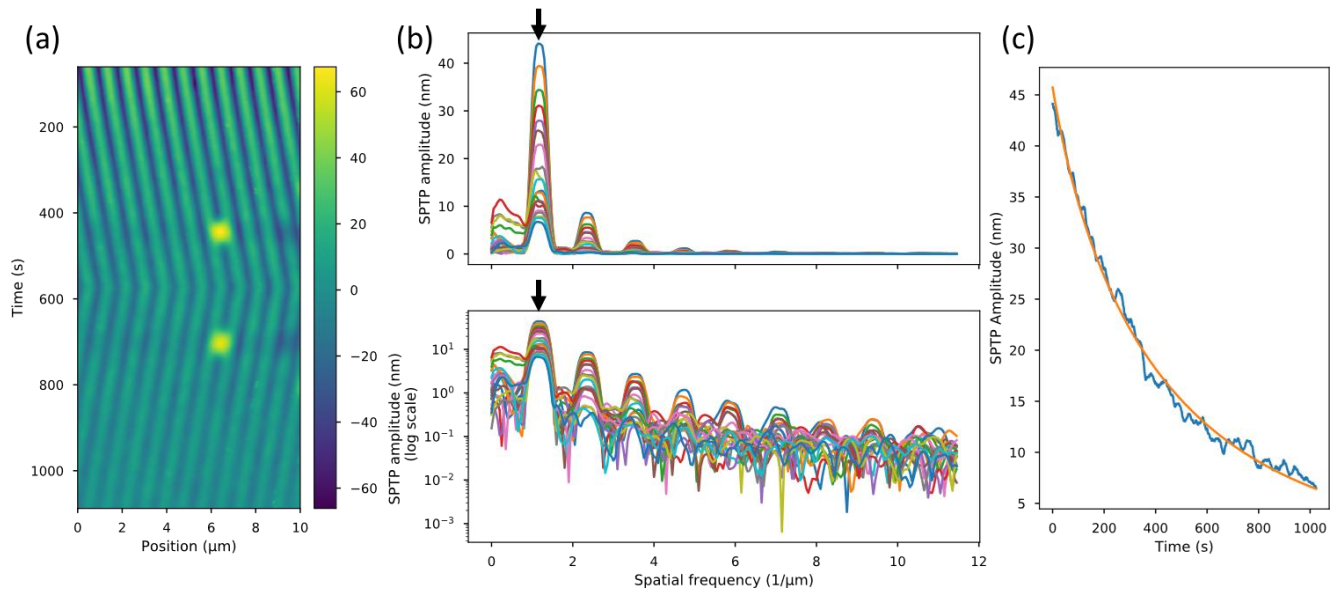


Figure 4. Decay of a nanopatterned film of PMMA with 20 % mass fraction bare SiO₂ NP at 125 °C with a 152 nm h_R . (a) Sequential height maps depicting the height decay as a function of time (b) Spectral analysis yielding sinusoidal features quantified by “spectral average peak to peak (SPTP) amplitude” as a function of the spatial frequency. (c) Tracking the primary peak frequency as function of time yields a height decay curve. Solid orange line depicts a stretched exponential fit to the data.

Utilizing the approach described above, various parameters affecting the pattern decay were investigated such as the decay temperature, h_R and type of nanoparticle, NP, added (PMMA grafted SiO₂ NP compared to unmodified bare SiO₂ NP). Figures 5a-c display SPTP amplitude decay

curves obtained from spectral analysis of the *in-situ* heated AFM images. Figure 5a shows the effect of decay temperature (for a fixed NP loading and residual layer thickness), where the decay rate of the patterned nanofeature increases as the exposure temperature increases. In Figure 5b, the effect of h_R is examined, and we observe that the decay kinetics are faster when the residual layer thickness increases. The reflow of the imprinted nanostructure speeds up as the residual thickness of the film increases due to a sharp decrease in the relaxation time as the mean thickness of the film increases as predicted by the lubrication approximation^{10,30}. Figure 5c demonstrates that the addition of unmodified bare NPs leads to the slowest decay kinetics compared to the grafted NPs due to the attractive interactions between the unmodified NP and the matrix chains.

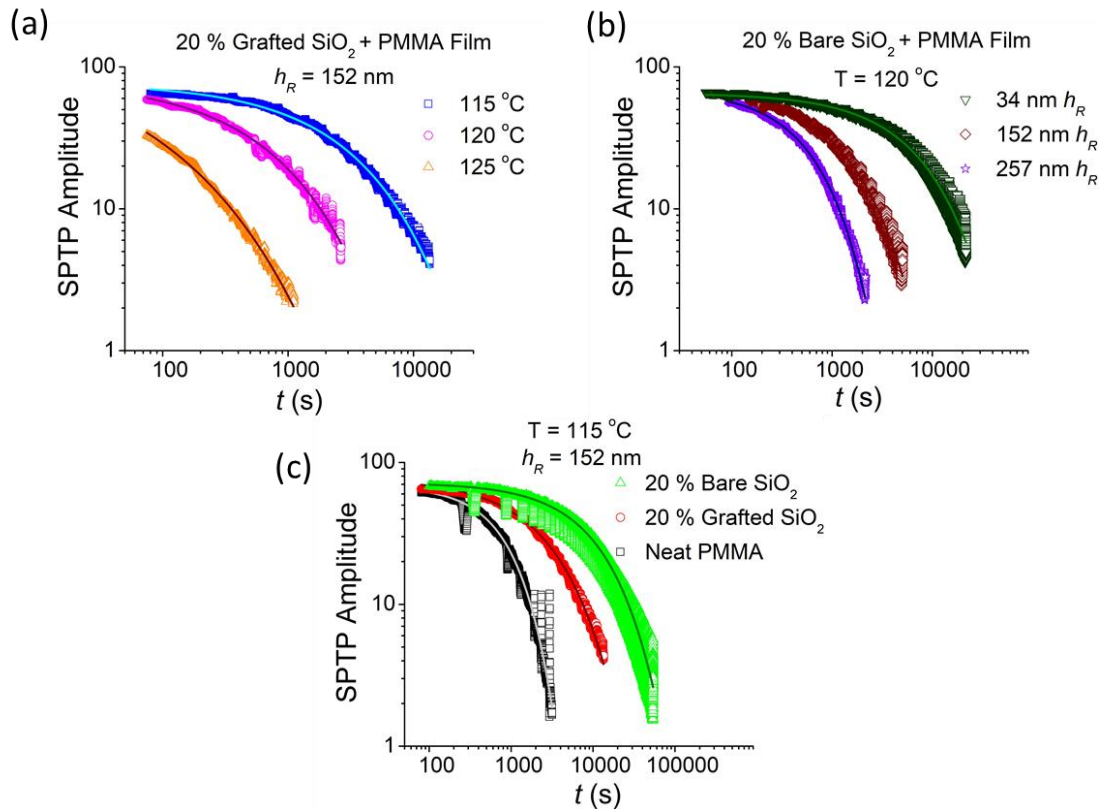


Figure 5. SPTP amplitude decay plots achieved from spectral analysis of the *in-situ* heated AFM images. (a) Effect of temperature for a 20 % filled (mass fraction relative to the PMMA matrix) grafted SiO₂ NP film for a h_R of 152 nm where increasing the temperature yields a faster decay

rate. (b) Effect of h_R underneath the patterned features for a 20 % filled (mass fraction relative to the PMMA matrix) bare SiO₂ NP film at 120 °C, depicting the faster reflow rate of the nanofeatures as the h_R increases. (c) Effect of particle system at a decay temperature of 115 °C for a h_R of 152 nm where bare SiO₂ NP features decays the slowest. Solid lines represent the stretched exponential fits to the data.

To quantify the relaxation dynamics of the pattern decay *via in-situ* heated AFM, SPTP amplitude decay plots (obtained from the spectral analysis) were fit to a stretched exponential function as shown in Figures 5a-c yielding τ and β . Arrhenius plots (τ as a function of $1/T$) and β of the pattern relaxation process for h_R 34 nm, 152 nm, and 257 nm are shown in Figure S1 (see Supplementary Information). β lies between 0.63 and 1.07 for neat PMMA films, between 0.36 and 1.08 for 20 % grafted SiO₂ NP (w.r.t. matrix mass) filled films, and between 0.3 and 1 for 20 % bare SiO₂ NP (w.r.t. matrix mass) filled films for all h_R investigated. Figures 6a-c show the τ of the pattern relaxation process as a function of the reduced glass transition temperature (T_g/T) for residual layer thicknesses (h_R) of 34 nm, 152 nm and 257 nm, respectively. The T_g of the PMMA matrix and the composites were determined *via* ellipsometry (see experimental section and Supporting information Figure S2 and S3). It can be seen from Figures 6a and 6b the relaxation kinetics are slowest for the bare SiO₂ NP, followed by the grafted SiO₂ NP and finally the neat PMMA. We believe that the pattern relaxation slows down due to strong attractive interactions between the matrix and the bare NP, leading to slower pattern decay kinetics. This specific result of the additive system will be explored in detail in a future study. One interesting thing to note here is the relaxation trends in Figure 6c for the h_R of 257 nm. Here, we see the effective relaxation time for the grafted SiO₂ NP film is almost comparable to the bare SiO₂ NP film. The effect of the type of additive added on the nanofeature stability was highly suppressed as the h_R was increased to 257 nm. This behaviour can be attributed to a higher reflow of the imprinted pattern (as predicted

by the lubrication approximation^{10,30}) into the bulk of the film and the NP interaction with the matrix plays a very small or insignificant role here as the majority volume of the film actually lies underneath the pattern. Confinement driven NP partitioning has been reported before where the NP can move to specific regions in a pattern dependent on the initial thickness of the film and the grafted polymer chain length.³¹ For the h_R , the particle system and the confining dimensions investigated in this study, we do not believe we have any selective partitioning of the NP within the pattern (which can influence heterogenous relaxation behaviour) and that the NP are well-dispersed throughout the thickness of the film.

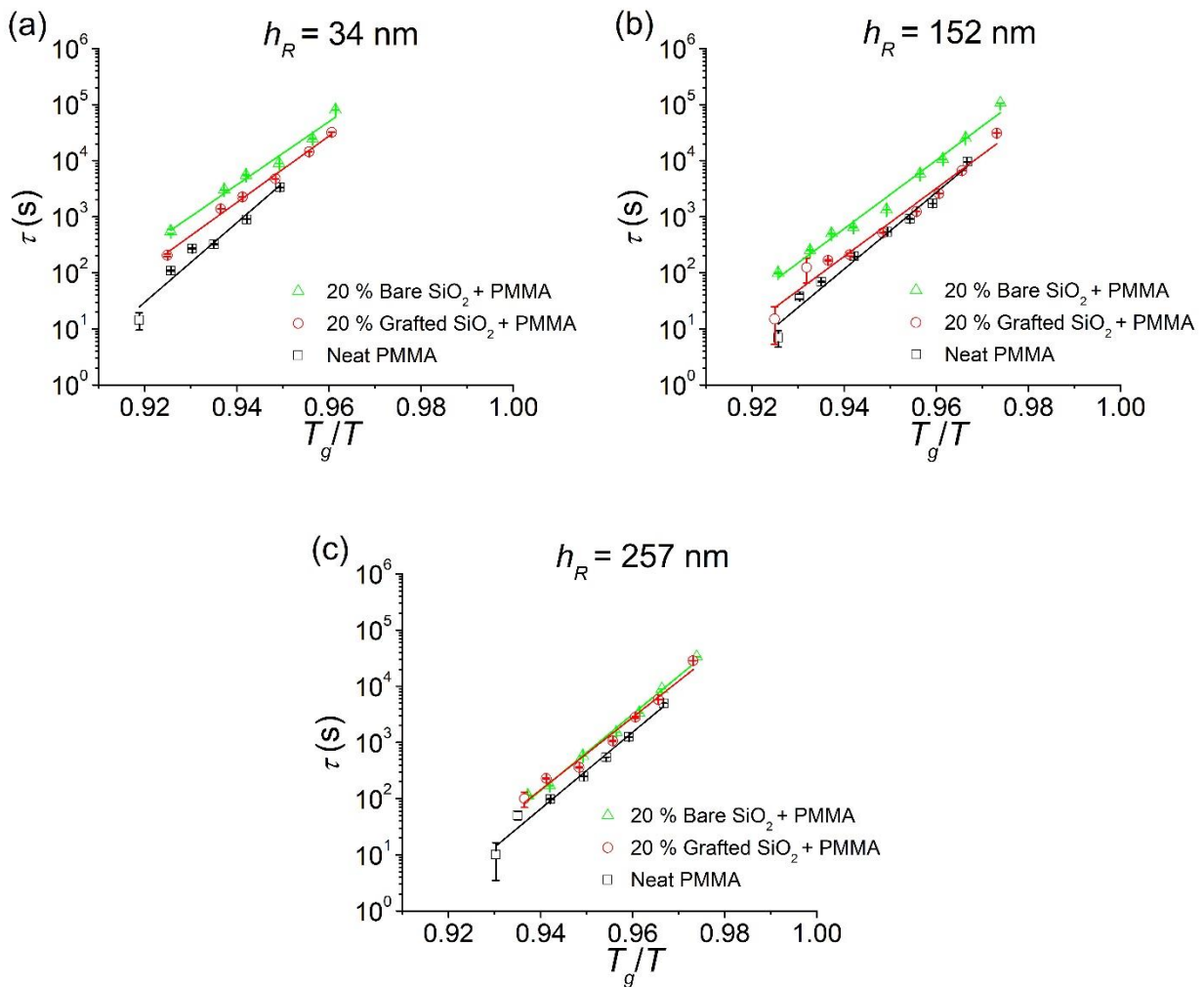


Figure 6. Relaxation time, τ as a function of T_g/T for (a) $h_R = 34$ nm (b) $h_R = 152$ nm (c) $h_R = 257$ nm respectively. Solid lines represent linear fits to the data.

It is important to note here that *in-situ* heated AFM technique enabled us to probe the effect of h_R on pattern decay of a very low molecular mass PMMA (3 kg/mol, $5\times$ smaller than the entanglement molecular mass of PMMA). Patterned films with higher h_R , in any case, decay much faster (> 9 - 10 times faster dependent on the decay temperature) than lower h_R films. Capturing this fast decay process *ex-situ* can be quite cumbersome and plagued with very low reproducibility of the decay kinetics. *In-situ* heated AFM measurements enabled the investigation of higher h_R films by delivering a high density of decay data points to capture the fast relaxation rate confidently. A comparison of decay data for an imprinted film captured *via ex-situ* AFM¹³ and *in-situ* AFM is shown in Figure S4, where a significant difference in the data density can be seen. Another advantage of using *in-situ* AFM as a measurement technique for nanopattern decay is the instrument's inherent flexibility in changing the stimulus driving the pattern decay; for example, the kinetics of imprinted organic nanofeature decay can change under exposure to various solvents (and their mixtures), electric charge, mechanical force, heat etc. The surface topography data collected is essentially the same, therefore the line-by-line spectral analysis approach depicted here would be identical for any stimulus-driven height decay being investigated, making this technique highly versatile.

Conclusion

We demonstrate *in-situ* heated AFM as a robust characterization tool for tracking the thermal induced decay of neat and composite patterned polymer films. Continuous scanning of the patterned film with a fixed scan frequency of 1 Hz enabled the capture of pattern decay at a

reasonable high temporal resolution of 1 s. Spectral analysis of each scan line provides direct insight in to the shape evolution of the pattern and can be used to quantify the decay of the pattern. It was seen that films with the lowest h_R and with unmodified SiO₂ NP decayed the slowest. For patterned films with highest h_R at all the temperatures investigated (above the T_g), the NP additive system (grafted SiO₂ NP and unmodified SiO₂ NP) played an insignificant role in reinforcing the patterned films as the relaxation times were almost comparable. As we have shown, this *in-situ* AFM technique and the subsequent analysis procedure holds high promise to be used for capturing the decay of patterned organic nanofeatures as it can be used for any material system, any underlying residual layer (h_R), and any substrate and doesn't require any special sample preparation.

Experimental

Poly(methyl methacrylate) (PMMA), with a number average molecular mass (M_n) of 3.1 kg/mol and polydispersity, \mathcal{D} of 1.09 was purchased from Polymer Source (syndiotactic rich content > 79 %) and was used as received. The glass transition, T_g for the PMMA matrix was ≈ 97.2 °C determined *via* ellipsometry¹³. PMMA grafted SiO₂ NP, $M_{n, \text{grafted chains}} \approx 19.4$ kg/mol, $\mathcal{D} \approx 1.17$, grafting density ≈ 0.65 chains/nm² with an average radius of $7.7 (\pm 2)$ nm after grafting as measured by transmission electron microscopy (TEM), were synthesized using surface-initiated atom transfer radical polymerization^{32,33}. The glass transition of the composite containing 20 % (mass fraction relative to the matrix mass) PMMA grafted SiO₂ NP in the PMMA matrix is $99.7 (\pm 0.1)$ °C determined *via* ellipsometry as shown in Figure S2. Unmodified bare SiO₂ NP (nominal radius $\approx 4.5 (\pm 0.5)$ nm) were purchased from Nissan Chemicals and used as received. The glass transition of the composite containing 20 % (mass fraction relative to the matrix mass) unmodified

bare SiO₂ NP in the PMMA matrix is 100.3 (\pm 0.5) °C determined *via* ellipsometry as shown in Figure S3.

Neat and composite PMMA solutions in acetone for unmodified SiO₂ NP and toluene for grafted SiO₂ NP were prepared with 20 % NP concentration with respect to the matrix mass. The solutions were then blade coated onto a clean ultraviolet ozone treated silicon substrate and the thickness of the films was measured by spectral reflectometry (F-20 Ultraviolet Thin Film Analyzer; Filmetrics, Inc.). The thickness of the neat PMMA and PMMA composite films before imprinting was 109 (\pm 4) nm, 227 (\pm 8) nm and 332 (\pm 7) nm to yield residual thickness (h_R) of 34 (\pm 4) nm, 152 (\pm 8) nm and 257 (\pm 7) nm respectively. TEM images indicating the dispersion of 20 % NP concentration with respect to the matrix mass for both unmodified bare SiO₂ NP and PMMA grafted SiO₂ NP can be seen in Figure S5 for a non-patterned as-cast film (film thickness of approximately 109 nm) . Cross-linked poly(dimethylsiloxane) (PDMS) (purchased from Dow, Sylgard 184 Silicone elastomer kit and used as received) elastomer layers (thickness \approx 1 mm, 20:1 base to curing agent) were made by casting against on Edmund Optics diffraction grating, pitch \approx 850 nm, height difference $\Delta h \approx$ 150 nm, and curing at 120 °C for 2 h. The PDMS elastomeric stamps were placed in contact with the blade-coated films, and the assembly was heated at 180 °C for 1 h to transfer the pattern *via* mold filling by capillary forces. Small samples were diced from the patterned films and used subsequently for the *in-situ* measurements.

In-situ heated AFM experiments were performed on a Dimension Icon (Bruker) equipped with a heat stage (Bruker), and the imaging was performed in tapping mode. Decay experiments were conducted at temperatures between 110 °C and 130 °C. The samples were small enough (low thermal mass) such that they equilibrated rapidly ($<$ 1 min) on the AFM heat stage within the delay time (t_D) observed to move the sample under the AFM head and engage the tip onto the

surface ($t_D \approx 45$ s to 90 s). We employed the automated sample stage and a reduced SPM safety height (50 μm) to speed up the time required to engage the tip onto the sample surface. The surface topography of the patterned samples was captured continuously at a scan rate of 1 Hz. Continuous scanning was stopped manually when the pattern height trace reached < 10 nm.

A script was written in Python to process Nanoscope data files using the Numpy and Scipy libraries.³⁴ After parsing the headers and loading the Z-sensor height maps, the images are concatenated, alternately flipping the images such that each line is sequential in time. For each line, the data are detrended with a linear fit, windowed using a “flattop” profile and zero-padded by a factor of 2 to precisely locate (*via* Fourier interpolation) and accurately measure (*via* flattop windowing) peak amplitudes. The frequency of the fundamental mode is selected by choosing the frequency of the maximum amplitude of the first scan of each dataset. Due to imperfections in the imprint, this may not be the actual maximum of each individual periodogram. The peak amplitudes were converted from mean squared power (P) to average peak-to-peak (SPTP) amplitude by the function $SPTP=(2P)^{0.5}$. Lines that were identified as containing pattern defects large enough to bias the SPTP measurement were manually eliminated from the fit by scaling the amplitude residuals by infinity, effectively setting those error residuals to zero. These lines were chosen liberally and, in some cases (as in Figure 4), lines were eliminated that would have had almost no effect on the resultant fit parameters, while in other cases, the eliminated lines would have significantly biased the stretched exponential fit. The SPTP amplitude at the fundamental frequency is then fitted using the Levenberg-Marquardt nonlinear least-squares algorithm to a stretched exponential function as described in equation 2 as in the work by Alvine, et al.³⁵ and Karim, et al.¹⁴ The fit was bounded to positive values for the initial amplitude (A_0), relaxation time (τ), and stretching exponent (β). The weight of the fits was determined by estimating the noise

amplitude of the data (≈ 50 pm) and scaling the amplitude residuals by that value. Parameter error estimates were generated using the covariance matrix at the optimal parameters and represent one standard uncertainty.

Author Information

Corresponding Authors:

*(R.J.S.) richard.sheridan@duke.edu

*(C.M.S) chris.stafford@nist.gov

ORCID

Sonal Bhadauriya: 0000-0002-2598-0848

Jianan Zhang: 0000-0003-3195-9882

Michael R. Bockstaller: 0000-0001-9046-9539

Alamgir Karim: 0000-0003-1302-9374

Richard J. Sheridan: 0000-0002-8944-8076

Christopher M. Stafford: 0000-0002-9362-8707

Present address:

(J.Z.) School of Chemistry and Chemical Engineering and Institute of Physical Science and Information Technology, Anhui University, Hefei 230601, China.

(R.J.S.) Department of Mechanical Engineering and Materials Science, Duke University, Durham, NC 27708, United States

Funding Sources

A.K. and M.R.B. would like to acknowledge DOE (BES) award DE-SC0018854 for funding of this project.

Acknowledgements

We thank Dr. Jack F. Douglas at National Institute of Standards and Technology for his valuable insights.

Notes

Certain commercial materials and equipment are identified to specify adequately the experimental procedure. In no case does such identification imply recommendation by the National Institute of Standards and Technology nor does it imply that the material or equipment identified is necessarily the best available for this purpose. The authors declare no competing financial interest.

Supporting Information

Arrhenius plots of relaxation times as a function of nanoparticle system and residual layer thickness; measurement of the glass transition temperature of each nanocomposite thin film; comparison of in-situ decay curves vs. ex-situ decay curves; TEM images of nanoparticle dispersion in the nanocomposite thin films.

References

- (1) Anastasiadis, S. H.; Lygeraki, M. I.; Athanassiou, A.; Farsari, M.; Pisignano, D. Reversibly Photo-Responsive Polymer Surfaces for Controlled Wettability. *J. Adhes. Sci. Technol.* **2008**, *22* (15), 1853–1868.
- (2) Anastasiadis, S. H. Development of Functional Polymer Surfaces with Controlled Wettability. *Langmuir* **2013**, *29*, 9277–9290.
- (3) Ertürk, G.; Mattiasson, B. Molecular Imprinting Techniques Used for the Preparation of Biosensors. *Sensors* **2017**, *17* (2), 1–17.
- (4) Devaraju, N. S. G. K.; Unger, M. A. Pressure Driven Digital Logic in PDMS Based Microfluidic Devices Fabricated by Multilayer Soft Lithography. *Lab Chip* **2012**, *12* (22), 4809–4815.
- (5) Nallapaneni, A.; Shawkey, M. D.; Karim, A. Specular and Diffuse Reflectance of Phase-Separated Polymer Blend Films. *Macromol. Rapid Commun.* **2017**, *38*, 1600803.
- (6) Zhou, B.; Wang, L.; Li, S.; Wang, X.; Hui, Y. S.; Wen, W. Universal Logic Gates via Liquid-Electronic Hybrid Divider. *Lab Chip* **2012**, *12*, 5211–5217.
- (7) Lenz, T.; Zhao, D.; Richardson, G.; Katsouras, I.; Asadi, K.; Glaber, G.; Zimmermann, S. T.; Stingelin, N.; Roelofs, W. S. C.; Kemerink, M.; Blom, P. W. M.; De Leeuw, D. M. Microstructured Organic Ferroelectric Thin Film Capacitors by Solution Micromolding. *Phys. Status Solidi Appl. Mater. Sci.* **2015**, *212* (10), 2124–2132.
- (8) Tabatabai, A.; Fassler, A.; Usiak, C.; Majidi, C. Liquid-Phase Gallium – Indium Alloy Electronics with Microcontact Printing. *Langmuir* **2013**, *29*, 6194–6200.
- (9) Rogers, J. A.; Bao, Z.; Dodabalapur, A.; Makhija, A. Organic Smart Pixels and Complementary Inverter Circuits Formed on Plastic Substrates by Casting and Rubber

- Stamping. *IEEE Electron Device Lett.* **2000**, *21* (3), 100–103.
- (10) Teisseire, J.; Revaux, A.; Foresti, M.; Barthel, E. Confinement and Flow Dynamics in Thin Polymer Films for Nanoimprint Lithography. *Appl. Phys. Lett.* **2011**, *98*, 013106.
- (11) Alvine, K. J.; Ding, Y.; Douglas, J. F.; Ro, H. W.; Okerberg, B. .; Karim, A.; Lavery, K. A.; Lin-Gibson, S.; Soles, C. L. Effect of Fluorosurfactant on Capillary Instabilities in Nanoimprinted Polymer Patterns. *J. Polym. Sci. Part B Polym. Phys.* **2009**, *47*, 2591–2600.
- (12) Alvine, K. J.; Ding, Y.; Douglas, J. F.; Ro, H. W.; Okerberg, B. C.; Karim, A.; Soles, C. L. Capillary Instability in Nanoimprinted Polymer Films. *Soft Matter* **2009**, *5* (15), 2913–2918.
- (13) Bhadauriya, S.; Wang, X.; Pitliya, P.; Zhang, J.; Raghavan, D.; Bockstaller, M. R.; Stafford, C. M.; Douglas, J. F.; Karim, A. Tuning the Relaxation of Nanopatterned Polymer Films with Polymer-Grafted Nanoparticles: Observation of Entropy – Enthalpy Compensation. *Nano Lett.* **2018**, *18*, 7441–7447.
- (14) Ding, Y.; Ro, H. W.; Germer, T. A.; Douglas, J. F.; Okerberg, B. C.; Karim, A.; Soles, C. L. Relaxation Behavior of Polymer Structures Fabricated by Nanoimprint Lithography. *ACS Nano* **2007**, *1* (2), 84–92.
- (15) Moore, A. L.; Shi, L. Emerging Challenges and Materials for Thermal Management of Electronics. *Mater. Today* **2014**, *17* (4), 163–174.
- (16) Hirai, Y.; Konishi, T.; Yoshikawa, T.; Yoshida, S. Simulation and Experimental Study of Polymer Deformation in Nanoimprint Lithography. *J. Vac. Sci. Technol. B Microelectron. Nanom. Struct. Process. Meas. Phenom.* **2004**, *22* (6), 3288–3293.
- (17) Hirai, Y.; Yoshida, S.; Takagi, S.; Tanaka, Y.; Yabe, H.; Sasaki, K.; Sumitani, H.;

- Yamamoto, K. High Aspect Pattern Fabrication by Nano Imprint Lithography Using Fine Diamond Mold. *Jpn. J. Appl. Phys.* **2003**, *42* (1, 6B), 3863–3866.
- (18) Lee, H. J.; Soles, C. L.; Ro, H. W.; Jones, R. L.; Lin, E. K.; Wu, W. L.; Hines, D. R. Nanoimprint Pattern Transfer Quality from Specular X-Ray Reflectivity. *Appl. Phys. Lett.* **2005**, *87*, 26311.
- (19) Wang, C.; Jones, R. L.; Lin, E. K.; Wu, W. L.; Leu, J. Small Angle X-Ray Scattering Measurements of Lithographic Patterns with Sidewall Roughness from Vertical Standing Waves. *Appl. Phys. Lett.* **2007**, *90*, 193122.
- (20) Hu, T.; Jones, R. L.; Wu, W. L.; Lin, E. K.; Lin, Q.; Keane, D.; Weigand, S.; Quintana, J. Small Angle X-Ray Scattering Metrology for Sidewall Angle and Cross Section of Nanometer Scale Line Gratings. *J. Appl. Phys.* **2004**, *96* (4), 1983–1987.
- (21) Jones, R. L.; Hu, T.; Lin, E. K.; Wu, W. L.; Kolb, R.; Casa, D. M.; Bolton, P. J.; Barclay, G. G. Small Angle X-Ray Scattering for Sub-100 Nm Pattern Characterization. *Appl. Phys. Lett.* **2003**, *83* (19), 4059–4061.
- (22) Jones, R. A. L.; Soles, C. L.; Lin, E. K.; Hu, W.; Reano, R. M.; W.Pang, S.; Weigand, S. J.; Keane, D. T.; Quintana, J. P. Pattern Fidelity in Nanoimprinted Films Using Critical Dimension Small Angle X-Ray Scattering. *J. Microlithogr. Microfabr. Microsystems* **2006**, *5* (1), 013001.
- (23) Wang, C.; Jones, R. L.; Lin, E. K.; Wu, W.-L.; Rice, B. J.; Choi, K. W.; Thompson, G.; Weigand, S. J.; Keane, D. T. Characterization of Correlated Line Edge Roughness of Nanoscale Line Gratings Using Small Angle X-Ray Scattering. *J. Appl. Phys.* **2007**, *102*, 024901.
- (24) Sunday, D. F.; List, S.; Chawla, J. S.; Kline, R. J. Determining the Shape and Periodicity

- of Nanostructures Using Small-Angle X-Ray Scattering. *J. Appl. Crystallogr.* **2015**, *48* (5), 1355–1363.
- (25) Chai, Y.; Salez, T.; A. Forrest, J. Using Mw Dependence of Surface Dynamics of Glassy Polymers to Probe the Length Scale of Free-Surface Mobility. *Macromolecules* **2020**, *53* (3), 1084–1089.
- (26) Patrick, H. J.; Germer, T. A.; Ding, Y.; Ro, H. W.; Richter, L. J.; Soles, C. L. In Situ Measurement of Annealing-Induced Line Shape Evolution in Nanoimprinted Polymers Using Scatterometry. In *Proceedings of the SPIE Conference on Alternative Lithographic Technologies. SPIE vol. 7271*; 2009; pp 1–11.
- (27) Ding, Y.; Ro, H. W.; Douglas, J. F.; Jones, R. L.; Hine, D. R.; Karim, A.; Soles, C. L. Polymer Viscoelasticity and Residual Stress Effects on Nanoimprint Lithography. *Adv. Mater.* **2007**, *19*, 1377–1382.
- (28) Suh, K. Y.; Lee, H. H. Capillary Force Lithography: Large-Area Patterning, Self-Organization, and Anisotropic Dewetting. *Adv. Funct. Mater.* **2002**, *12* (6–7), 405–413.
- (29) Salez, T.; McGraw, J. D.; Bäumchen, O.; Dalnoki-Veress, K.; Raphaël, É. Capillary-Driven Flow Induced by a Stepped Perturbation atop a Viscous Film. *Phys. Fluids* **2012**, *24* (10), 102111.
- (30) Leveder, T.; Landis, S.; Davoust, L. Reflow Dynamics of Thin Patterned Viscous Films. *Appl. Phys. Lett.* **2008**, *92*, 013107.
- (31) Zhang, R.; Lee, B.; Stafford, C. M.; Douglas, J. F.; Dobrynin, A. V.; Bockstaller, M. R.; Karim, A. Entropy-Driven Segregation of Polymer-Grafted Nanoparticles under Confinement. *Proc. Natl. Acad. Sci.* **2017**, *114* (10), 2462–2467.
- (32) Pyun, J.; Matyjaszewski, K. Synthesis of Nanocomposite Organic/Inorganic Hybrid

- Materials Using Controlled/“Living” Radical Polymerization. *Chem. Mater.* **2001**, *13* (10), 3436–3448.
- (33) Matyjaszewski, K.; Tsarevsky, N. V. Nanostructured Functional Materials Prepared by Atom Transfer Radical Polymerization. *Nat. Chem.* **2009**, *1*, 276–288.
- (34) Oliphant, T. Python for Scientific Computing. *Comput. Sci. Eng.* **2007**, *9* (3), 10–20.
- (35) Ding, Y.; Qi, H. J.; Alvine, K. J.; Ro, H. W.; Ahn, D. U.; Lin-Gibson, S.; Douglas, J. F.; Soles, C. L. Stability and Surface Topography Evolution in Nanoimprinted Polymer Patterns under a Thermal Gradient. *Macromolecules* **2010**, *43* (19), 8191–8201.

TOC Image

